https://dx.doi.org/10.21577/0103-5053.20220091

J. Braz. Chem. Soc., Vol. 34, No. 1, 92-102, 2023

Article

Bimetallic Au-Pd/α-MoO_3 Catalyst with High Oxygen Vacancies for Selective Oxidation of Cinnamyl Alcohol

Renilma C. Sousa,[a] Jussara M. da Silva,[a] Jean C. S. Costa,[,a] Carla V. R. de Moura[a] and Edmilson M. de Moura[a]*

[a]*Departamento de Química, Universidade Federal do Piauí, Campus Universitário Ministro Petrônio Portella, Ininga, 64049-550 Teresina-PI, Brazil*

Supported Au-Pd nanoparticles (NPs) have been extensively studied in alcohol oxidation reactions. However, few studies use reducible metal oxides as support, which can activate oxygen molecules and boost the selectivity of the reaction. In this work, Au-Pd NPs were supported on α-MoO_3 and evaluated in the selective oxidation of cinnamyl alcohol without solvent. The Fourier transform infrared spectroscopy (FTIR), Raman spectroscopy, and X-ray photoemission spectroscopy (XPS) analyses showed that the catalyst is richer in oxygen vacancies than the support, being probably responsible for the stability of the NPs (average size 4.62 ± 0.15 nm) and the high conversion and selectivity for the oxidation of cinnamyl alcohol. Furthermore, experiments have shown that the Au:Pd molar ratio influences the catalytic performance and can be optimized by controlling temperature, pressure, and reaction time. The catalyst proved to be active and selective for cinnamaldehyde in short reaction times. It showed satisfactory performance at 30 min and its best activity at 1 h with 94% conversion and 87% selectivity, without loss of activity and selectivity after four runs under the same reaction conditions.

Keywords: alcohol oxidation, Au-Pd nanoparticles, cinnamyl alcohol, MoO_3

Introduction

The oxidation of alcohols is currently one of the most important processes in the chemical industry, contributing to the production of aldehydes, widely used in the manufacture of fine chemicals, which play an important role in the pharmaceutical, agrochemical, and cosmetics industries.[1,2] However, this process has little selectivity and low conversions, making it challenging to develop new catalysts with highly active and selective characteristics to minimize this disadvantage.[3-5]

Aerobic oxidation of cinnamyl alcohol has stood out as a model reaction for alcohol oxidation.[6-8] Because it is an allylic alcohol, the presence of the alkene and primary alcohol functionalities make the chemoselective oxidative process challenging. Keresszegi *et al.*[9] demonstrated the existence of a complex reaction network, resulting in the formation of several products, which can be influenced by the composition of the catalyst, the reaction atmosphere, the solvent, and the temperature, which are factors that can control the selectivity.

Since the discovery of the catalytic properties of gold by Haruta *et al.*[10] in the oxidation of CO, this metal has brought interest in several areas, including the selective oxidation of alcohols.[11,12] Systematic studies[10,13] demonstrate that monometallic gold catalysts generally depend on the size of the nanoparticles (NPs), structure, preparation conditions of the metal, the catalyst, and a primary medium to exhibit catalytic activity. New studies[5,14,15] have reported a catalytic improvement in bimetallic systems with gold from the effect provided by a second metal, such as palladium, a result associated with a synergistic effect between the two metals.

Supports for NPs play essential roles in the synthesis and application of catalysts. Nonreducible supports such as SiO_2 and ZrO_2 present themselves as efficient catalysts for the oxidation processes of alcohols in aldehyde.[16,17] However, the catalysts show enhanced activity when these NPs are supported on reducible metallic oxides. That is attributed to collaborative effects between the support and the metallic nanoparticles from electronic interactions due to the physicochemical properties of the support surface and the ability of these materials to activate oxygen molecules.[18-21] Among them, we have the molybdenum oxide (MoO_3), for which three main polymorphs are known,

*e-mail: jean-cla@ufpi.edu.br
Editor handled this article: Jaísa Fernandes Soares

the α-MoO_3 (orthorhombic), β-MoO_3 (monoclinic) and h-MoO_3 (hexagonal) phases, which the thermodynamically stable phase is orthorhombic.[20]

MoO_3 has been used in numerous applications, such as gas sensors supercapacitors. It has stood out in the heterogeneous catalysis for its redox properties and its ability to reversibly exchange lattice oxygen due to changes in the oxidation state Mo^{6+}/Mo^{5+}.[20,22-24]

Cinnamaldehyde, the target product, is an allylic aldehyde originating from the oxidation reaction of cinnamyl alcohol and is widely used as an additive in foods and perfumes.[8] The literature[25] reports that it is obtained through the oxidative dehydrogenation of alcohol. Its selectivity is also influenced by the competitive hydrogenation of the C=C bond or the C–O cleavage in the source alcohol and the decarbonylation of the desired aldehyde.[25] Benzaldehyde has been reported as a by-product in the oxidation reactions of cinnamyl alcohol through the process of auto-oxidation by a radical route, which consists of the main factor that alters the selectivity.[8,26,27] The auto-oxidation process is the oxidation without any catalyst, being a reaction that occurs in almost all oxidation processes, but is still frequently overlooked in the literature. This process can influence the selectivity of the desired product, and the choice of a catalyst can affect the activation of these oxidative routes preventing this process from happening.[26,27]

Here, we propose the synthesis of an Au-Pd NPs catalyst impregnated by deposition precipitation with urea in MoO_3. The system demonstrated that combining bimetallic NPs with the reducible support can provide a pronounced performance for the solvent-free oxidation of cinnamyl alcohol without adding any external base. In addition, the study and optimization of variables such as temperature, pressure, reaction time, and the molar ratio of Au:Pd favored the best conversion rates and selectivity for cinnamaldehyde and inhibited the auto-oxidation process. We also performed the complete characterization of the best catalyst for our proposals (Au:Pd molar ratio of 1:1) associated with the experimental data, explaining its catalytic performance. Furthermore, the stability of the catalyst was satisfactory, being analyzed in four runs without loss of activity.

Results and Discussion

Catalyst characterization

Bimetallic catalysts with different proportions of Au-Pd were coded for a better understanding and description in the text, with 2Au-Pd/α-MoO_3 as the catalyst that presents the Au-Pd molar ratio (1:0.5), and Au-Pd/α-MoO_3 as the catalyst with Au-Pd molar ratio (1:1) (Table S1, Supplementary Information (SI) section).

The crystalline structure of the synthesized samples was characterized by X-ray diffraction (XRD). The main reflections were identified with the aid of the crystallographic files acquired in the ICSD database (Inorganic Crystal Structure DataBase®). Figure 1 shows the XRD pattern of the MoO_3 sample. The diffraction pattern of the planes (020), (110), (040), (021), (111), and (060) correspond to the structure orthorhombic α-MoO_3 with a spatial group (*Pbmn*) and point symmetry group (D_{2h}), following the literature (ICSD 230018).[27,28]

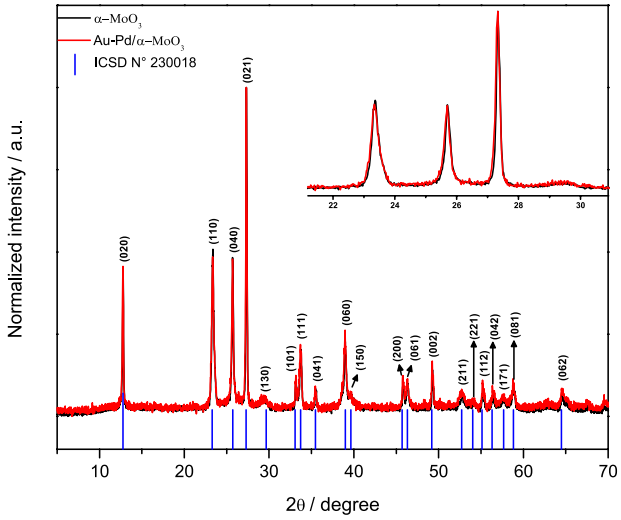

Figure 1. XRD patterns of α-MoO_3 and Au-Pd/α-MoO_3 samples.

The diffractogram also showed that the material is partially oriented in the reflections of (0k0) with k = 2, 4, and 6, which indicates that the oxide particles have a preferential orientation along the b-axis, resulting in anisotropic growth.[29] The X-ray patterns of the catalyst (Figure 1) show peaks that correspond to the α-MoO_3, with only slight shifts occurring in the a/b/c network parameter, indicating that no structural changes were induced in the support during the preparation of the catalyst. However, no signals attributed to the Au-Pd NPs can be observed, which can be related to small particle size and the relatively low concentrations of Au-Pd (1.6 wt.%, determined by inductively coupled plasma optical emission spectrometer (ICP-OES), Table S1) relative to MoO_3.

Figure 2 shows the spectroscopy Raman and Fourier transform infrared spectroscopy (FTIR) spectra of the material where several active modes are observed. The intense bands are attributed to the high crystallinity of the material, making it possible to identify the three main ones (994, 819, and 290 cm^{-1}) that are characteristic of

the layered orthorhombic structure according to the XRD analysis.[30]

The active Raman modes of MoO_3 appear in the frequency range of 1000 and 600 cm^{-1}, 400 to 200 cm^{-1}, and below 200 cm^{-1}, which correspond to the stretching, deformation, and lattice modes, respectively.[22,30,31] The band at 994 cm^{-1} is attributed to the vibrations of asymmetric stretching υ_{as}Mo=O of terminal oxygen. The intense band at 819 cm^{-1} originates from the vibrations of the symmetric stretching of doubly coordinated oxygen υMo–O–Mo from corner-shared oxygen at the vertices of two MoO_6 octahedra.[29] The bands at 665 and 470 cm^{-1} correspond to the asymmetric stretching vibration of the triply coordinated oxygen (υ_{as}Mo–O), originating from the edge-shared in common to three MoO_6 octahedra and bend, respectively.[30] The band at 290 cm^{-1} refers to O=Mo=O deformation mode.[32] The bands at 377 and 336 cm^{-1} correspond to O–Mo–O deformation (scissoring). The bands at 243, 217, and 195 cm^{-1} are attributed to the deformation of O=Mo=O. The band at 156 cm^{-1} comes from the deformation of $(O–Mo)_n$. The bands at 124 and 94 cm^{-1} correspond to the MoO_4 translational chain mode.[30] The Raman spectra of the support and the catalyst are very similar, as shown in Figure 2a. However, it is possible to observe a shift of bands in the Raman spectrum of the catalyst. The displacements of the Raman vibrational modes in 994 and 665 cm^{-1} to 990 and 662 cm^{-1} and from 290 to 281 cm^{-1} can be explained by the formation of oxygen vacancies, allowing the Mo atom to move towards the terminal oxygen due to oxygen loss.[32]

Figure 2b illustrates the FTIR spectrum of α-MoO_3 and the catalyst in 4000-400 cm^{-1}, where it is possible to observe the characteristic bands of the transition metal.[33] The displacements of the bands in Figure 2b can also be associated with oxygen vacancies when the metals are supported in α-MoO_3, as shown in the Raman spectroscopy analysis.

The influence of the metal charge deposited on the support was investigated through its surface changes. Thus, the textural characteristics of the samples were measured by the N_2 physisorption technique. According to the International Union of Pure and Applied Chemistry (IUPAC) classification, all the samples exhibit type IV isotherms (Figure S1, SI section), characteristic of mesoporous materials, and H3 type hysteresis loop, characteristic of slit-shaped pores.[34] Comparing the results obtained for the samples (Table 1), it is observed that the deposition of the metal nanoparticles on the support induces a decrease in pore volume and pore diameter due to the incorporation of Au-Pd NPs into their mesoporous channels.[35] There was also an increase of approximately 30% in the surface area of the catalyst concerning the support caused by the deposition of the metallic nanoparticles, proposing that the NPs activated the active sites present on the surface of the material.[36] This increase may be associated with an increase in the concentration of oxygen vacancies through electronic interactions between the particles and the support due to the high dispersion of the particles in the material.

The freshly prepared catalysts (2Au-Pd/α-MoO_3 and Au-Pd/α-MoO_3) were submitted to ICP-OES analysis to quantify the deposited metals. The results obtained (Table S1) verified that the deposition-precipitation with the urea method (DPU) did not provide a complete deposition of the metals on the supports. However, the actual levels deposited were satisfactory in both catalysts. In addition, the actual proportions and individual amounts of effectively deposited metals were also analyzed.

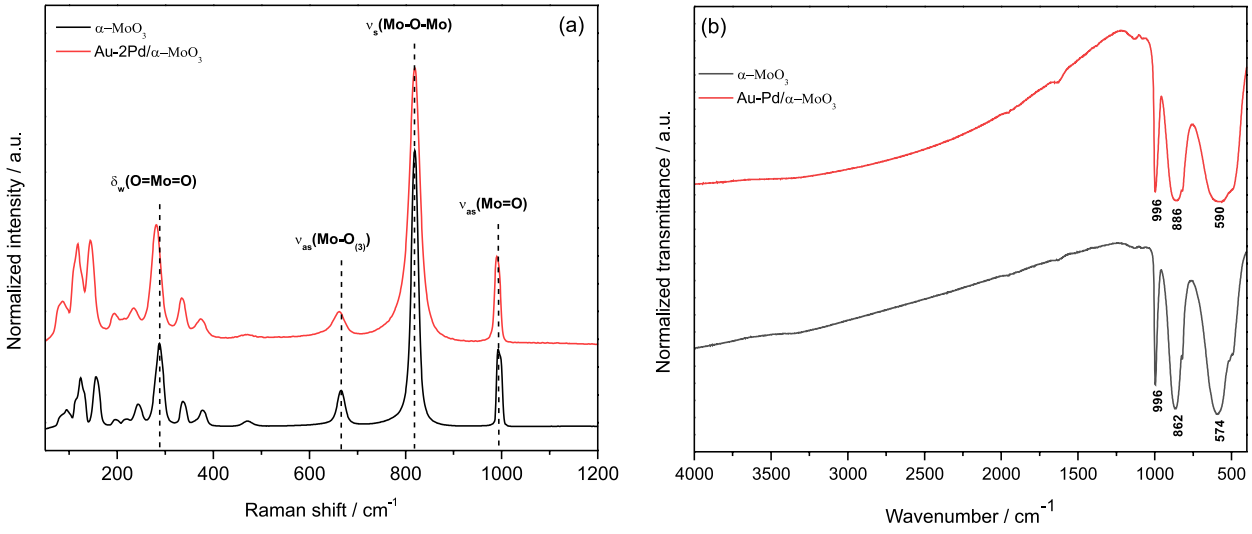

Figure 2. (a) Raman spectra and (b) FTIR (KBr) spectra of α-MoO_3 and Au-Pd/α-MoO_3.

Table 1. Chemical analysis and surface proprieties measured by N_2 physisorption of the catalysts

Catalyst	Au-Pd content[a] / wt.%	Surface area[b] / ($m^2 g^{-1}$)	V_t[c] / ($cm^3 g^{-1}$)	D_t[d] / nm
α-MoO_3	–	3.3843	0.025664	16.8086
Au-Pd/α-MoO_3	1.6	4.3908	0.023479	13.5385

[a]Metal content measured by inductively coupled plasma optical emission spectrometer (ICP-OES); [b]Brunauer-Emmett-Teller (BET) method; [c]total pore volume; [d]pore diameter calculated by Barrett-Joyner-Halenda (BJH) adsorption method.

The results revealed a metallic content slightly lower than the proposed theoretical load. The catalysts presented higher Au:Pd ratio values than expected, suggesting that the Au loading was more significant than Pd in both bimetallic catalysts. This phenomenon can be explained by the competitiveness between the gold and palladium species in the solution, promoting a repulsion of charges on the surface of the support and minimizing the deposition rates of the metals.[37]

Méndez *et al.*[38] also observed a lower deposition than the proposed theoretical rate of metallic nanoparticles (Pd, Pt, Ag, and Au) supported on TiO_2, using the deposition-precipitation method with urea. The authors suggested that the deviation could be due to the formation of soluble complexes that would be eliminated during the washing step.

The composition of the reused catalyst (Au-Pd/α-MoO_3(R)) was also analyzed. The results showed a lower metal content than in the newly prepared catalyst and a decrease in the Au:Pd ratio, indicating the leaching of metals during the reaction cycles, where there was a greater loss than in gold.

The morphology and microstructure of the samples were further characterized by scanning electron microscopy (SEM) and transmission electron microscopy (TEM) observations. Figures 3a and 3b give the representative SEM images of the samples, suggesting that the α-MoO_3 is composed of overlapping lamellar microplates, which are characteristics of the orthorhombic structure. The Au-Pd particles are equally distributed on the α-MoO_3 plates (Figures 3c and 3d). The low concentration of Au-Pd NPs (1.6 wt.%, determined by ICP-OES, Table S1) hampered the size definition of the particles by XRD. However, TEM analyses showed well-dispersed Au-Pd NPs with a mean diameter of 4.62 ± 0.15 nm (Figure 3e). The size of the nanoparticles and their high dispersion are influenced by the presence of oxygen vacancies in the support and the synthesis method of metallic particles.[7]

The samples were characterized by X-ray photoemission spectra (XPS) to obtain information concerning the chemical state and the composition of the material. The survey scan revealed the presence of Mo, O, and C for the support (Figure S2, SI section) and the signal of Mo, O, Au, Pd, and C on the spectrum of the catalyst (Figure S3, SI section), confirming the presence of the metal in the material. Furthermore, the presence of carbon is associated with the adventitious C on the surface of the material.

Figures 4a and 4b show the high-resolution spectra for Au 4f and Pd 3d. The binding energies (BE) of the Au 4f

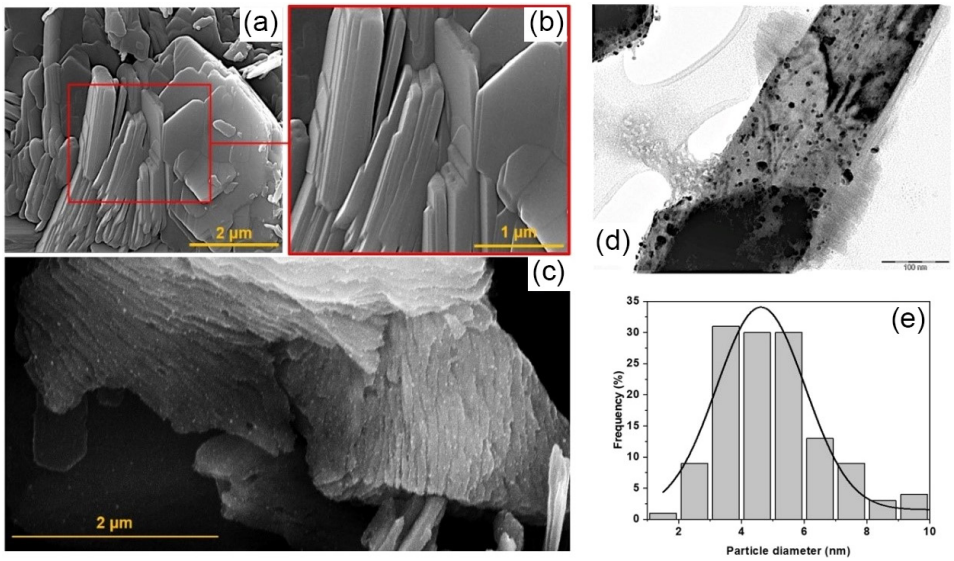

Figure 3. (a) Low-magnification and (b) high-magnification SEM images of α-MoO_3 samples; (c) low-magnification SEM images of Au-Pd/α-MoO_3 sample; (d) TEM image of Au-Pd/α-MoO_3 and (e) corresponding size distribution histogram.

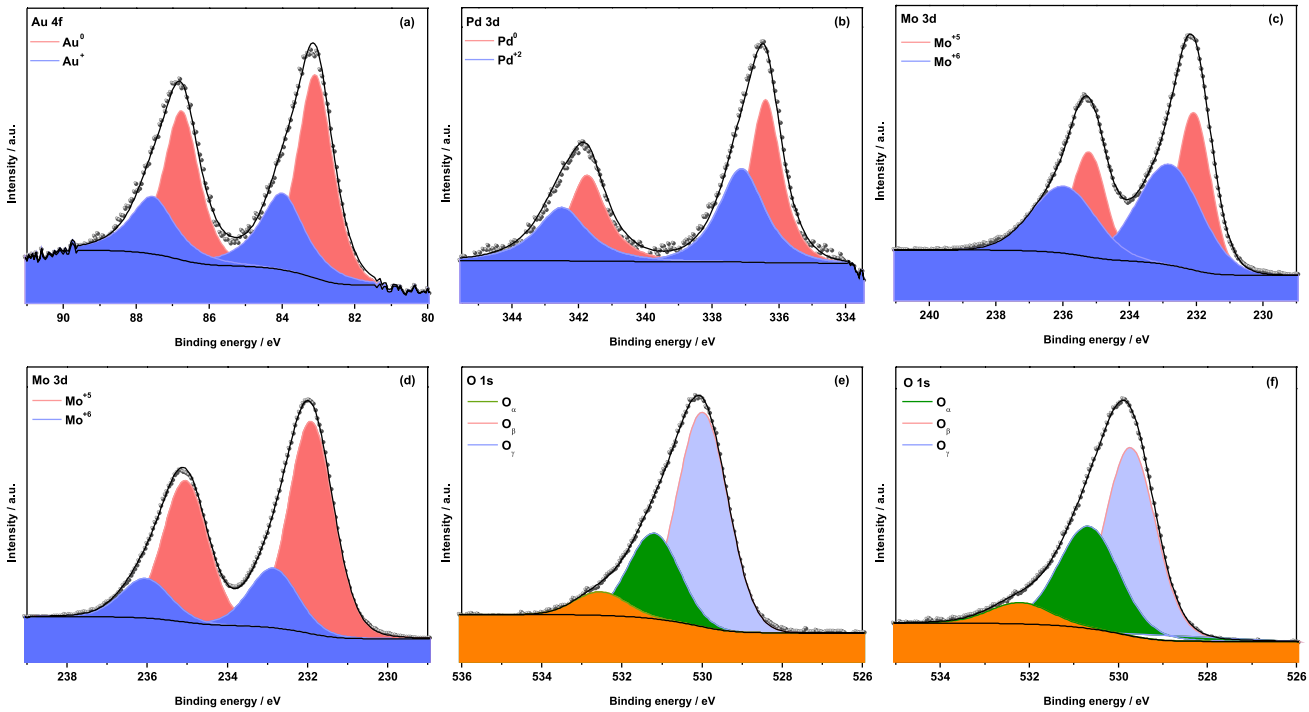

Figure 4. XPS spectra of (a) Au 4f, (b) Pd 3d, (c) Mo 3d support, (d) Mo 3d catalyst, (e) O 1s support, (f) O 1s catalyst levels. The black line represents the fitted spectrum, and the black dots are the background.

were measured at 83.1 eV (Au $4f_{7/2}$) and 86.8 eV (Au $4f_{5/2}$), suggesting Au^0 species and at 84.0 eV (Au $4f_{7/2}$) and 87.6 eV (Au $4f_{5/2}$) that can be attributed to Au^+ species.[39,40] The high-resolution Pd 3d XPS spectra deconvolution shows two palladium states. The binding energies at 336.4 eV (Pd $3d_{5/2}$) and 341.7 eV (Pd $3d_{3/2}$) are associated with Pd^0 species and at 337.1 eV (Pd $3d_{5/2}$) and 342.5 eV (Pd $3d_{3/2}$) to Pd^{2+} species.[41] For both metals, small deviations in the binding energy values were observed concerning the values typically reported in the literature for their respective pure metal components (Au^0 $4f_{7/2}$, 84.0 eV and Pd^0 $3d_{5/2}$, 335.0 eV). The negative peak deviation in BE for Au and positive peak shift in BE for Pd can be attributed to the formation of Au-Pd alloys from the electronic modification of Au species by Pd.[40] This organization of the particles agrees with what is observed in the TEM image of the material (Figure S4, SI section). The greatest contributions are from the metallic particles of Au^0 (65.0%) and Pd^0 (54.7%). The changes in the oxidation state of the components correspond to an electron transfer between Au to Mo ($Au + Mo^{6+} \rightarrow Au^+ + Mo^{5+}$) and Pd to Mo ($Pd + Mo^{6+} \rightarrow Pd^{2+} + Mo^{5+}$) due to strong interactions between AuPd and MoO_3, which may be related to the ability of the support (MoO_3) to supply oxygen to the nanoparticles, facilitating the formation of Au^+ and Pd^{2+} species.[42] Thus, the presence of noble metals increased the amount of surface oxygen in Au-Pd/α-MoO_3 when compared to MoO_3.

The Mo 3d XPS spectra for the supporting and catalyst are shown in Figures 4c and 4d. In the high-resolution spectra for Mo 3d of support, the peak at binding energies suggests that Mo^{6+} species predominates (Mo $3d_{5/2}$, 232.80 eV; Mo $3d_{3/2}$, 235.96 eV). The presence of Mo^{5+} species (Mo $3d_{5/2}$, 232.07 eV; Mo $3d_{3/2}$, 235.22 eV) is also observed. In the Mo 3d spectrum of the catalyst (Figure 4d), two Mo species were also observed, Mo^{6+} (Mo $3d_{5/2}$, 232.85 eV; Mo $3d_{3/2}$, 236.04 eV) and Mo^{5+} (Mo $3d_{5/2}$, 231.91 eV; Mo $3d_{3/2}$, 235.05 eV).[18]

According to the spectroscopic analyses, the significant increase in Mo^{5+} in the catalyst sample (Table S2, SI section) may be related to the electron transfer from nanoparticles to the support, leading to higher concentrations of oxygen vacancies. In Figures 4e and 4f, we can see the high-resolution spectrum for O 1s. The adjustment was performed with three energy individuals at 529.7 eV, attributed to lattice oxygen (O_α), at 530.7 eV associated with oxygen vacancies (O_β), and the peak at 532.2 eV is attributed to other weakly bound oxygen species (O_γ).[19] According to the XPS spectra analysis of the support and the catalyst for the O 1s level, it is possible to evaluate the oxygen vacancies concentration from the O_β/O_α ratio of the materials, where there is a higher concentration of oxygen vacancies in the catalyst (0.65) when compared to the support ratio (0.40), following the high rates of Mo^{5+} in the catalyst, as shown in Table S2.[19,40]

Experimental design for catalyst performance

Bimetallic catalysts at different Au-Pd molar ratios (1:0.5 and 1:1) and monometallic catalysts were applied in the oxidation reaction of cinnamyl alcohol. The experiments were investigated for their performance by applying oxidation reactions without adding solvent or base under an O_2 atmosphere. The selectivity of the reactions refers to the formation of cinnamaldehyde, benzaldehyde, and others up to 100%, corresponding to unidentified by-products, which were obtained by gas chromatography (CG) (Tables 2 and 3).

A blank test with the substrate without catalyst (Table 2, entry 1) has shown 19% conversion without any selectivity control (44% cinnamaldehyde, 54% benzaldehyde, and 2% other products). The same occurred when only the support (α-MoO_3) was submitted as a catalyst for the oxidation of the substrate under the same reaction conditions (Table 2, entry 2).

When the Au and Pd monometallic catalysts were given to the oxidation reaction (Table 2, entries 3 and 4), an increase in the conversion rate was observed concerning the support. However, the Pd/α-MoO_3 catalyst had better catalytic results suggesting a more significant interaction between the metallic particles and α-MoO_3, reinforcing its better catalytic performance concerning gold monometallic.

In this context, the performance of bimetallic catalysts was studied, in which two Au:Pd molar proportions were addressed. In the Au-Pd catalyst (1:0.5) (Table 2, entry 5), it was possible to observe an increase in conversion (70%) and greater control of selectivity, obtaining cininamaldehyde as the primary product (61%), but still presenting considerable quantities of other products. Thus, a new proportion with a higher amount of Pd was studied. Therefore, the Au-Pd/α-MoO_3 catalyst with an Au-Pd molar ratio of 1:1 (Table 2, entry 6) was tested, with a conversion rate of 94% and a higher selectivity for cinnamaldehyde (88%) and a decrease in the formation of benzaldehyde (11%), which is significantly less than the autocatalytic oxidation and catalytic oxidation using only the support, suggesting that the effect of inhibiting radical reaction pathways is related to the interaction of metallic particles with the support, and not just α-MoO_3. It can also be seen that the conversion and selectivity depend on the proportions of Au-Pd.

Teles *et al.*[43] reported that metal ions that can transfer only one electron, such as Co^{2+}/Co^{3+}, Mn^{2+}/Mn^{3+}, can divide hydroperoxides, preventing auto-oxidation. The presence of hydroperoxides are factors that initiate the autocatalytic process and the reaction temperature. The Au-Pd/α-MoO_3 catalyst seems to have similar properties when we verify the oxidation states of the species through XPS analysis. In this way, this catalyst appears to act as a radical trap inhibiting the auto-oxidation process. Evidence of this process is the reduction of benzaldehyde formation concerning the blank reaction and the sole presence of the support.[1]

This better result for bimetallic catalysts than the monometallic ones can be explained further due to the synergistic effect between the two metals. Similar effects have been reported by Dimitratos *et al.*[14] They obtained better results in bimetallic catalysts than their monologues when they submitted the 0.73% Au-0.27% Pd/AC catalyst (conversion of 72% in 2 h and selectivity for 85% cinnamaldehyde) oxidation of cinnamyl alcohol.

Based on the results obtained, further studies were carried out with the Au-Pd catalyst (1:1), obtained as the one with the best catalytic performance in the oxidation reaction of cinnamyl alcohol.

New experiments were carried out to optimize the reaction conditions for the chosen catalyst, subjecting it to investigative reactions under temperature and pressure variations (Table 3) to avoid auto-oxidation. We can notice that by increasing the temperature from 80 to 120 °C (Table 3, entries 1-3), there is an increase in the catalytic activity. However, there is a decrease in the selectivity of cinnamaldehyde, favoring the formation of benzaldehyde, suggesting that the auto oxidative path of the reaction is

Table 2. The oxidation reaction of cinnamyl alcohol[a]

entry	Catalyst	Molar ratio Au:Pd[b]	Conversion / %	Selectivity / %		
				Cinnamaldehyde	Benzaldehyde	Others
1	without catalyst	–	19	44	54	2
2	α-MoO_3	–	26	44	53	3
3	Au/α-MoO_3	–	41	55	41	4
4	Pd/α-MoO_3	–	66	49	47	4
5	2Au-Pd/α-MoO_3	1:0.5	70	61	35	4
6	Au-Pd/α-MoO_3	1:1	94	88	11	1

[a]Reaction conditions: 7.3 mmol of cinnamyl alcohol, 5.3 μmol of metal, catalysts/alcohol (1/1377), 4 bar of O_2, reaction temperature 100 °C, 1 h; [b]metal content measured by inductively coupled plasma optical emission spectrometer (ICP-OES).

Table 3. Oxidation reactions of cinnamyl alcohol using Au-Pd/α-MoO_3 catalyst[a]

entry	Pressure / bar	Temperature / °C	Conversion / %	Selectivity / %		
				Cinnamaldehyde	Benzaldehyde	Others
1	4	80	31	88	11	1
2	4	100	94	87	11	1
3	4	120	95	70	21	9
4	3	100	58	92	7	1
5	5	100	94	90	9	1

[a]Reaction conditions:7.3 mmol of cinnamyl alcohol, 5.3 μmol of metal, catalysts/alcohol (1/1377), 1 h.

triggered by the temperature rise, confirming the literature reports.[7,44] Thus, keeping the temperature at 100 °C, the pressure change from 3 to 5 bar was analyzed (Table 3, entries 2, 4, and 5) since the activity would not be efficient at lower pressures. Because of instrumental limitations, it was not explored in higher pressures.

The pressure effect is also a determining factor in catalytic activity. When investigating the performance of the catalyst at a pressure of 3 bar (Table 3, entry 4), a low conversion of alcohol is noted, but with significant control in the selectivity of the products. However, when the pressure is increased to 4 bar (Table 3, entry 2), it is possible to observe a marked increase in activity that remains almost unchanged at 5 bar (Table 3, entry 5) without presenting a significant difference in selectivity. With the increase in the pressure, there is an increase in conversion and a reduction in selectivity for cinnamaldehyde, suggesting that the formation of benzaldehyde is favored through the oxidative cleavage of the double bond C=C from the increase in pressure.[7,26] In this way, the best performance of the catalyst was established under the reaction conditions of 100 °C and 4 bar.

The reaction time optimization was evaluated under the previously established optimal conditions. Thus, the profile of alcohol conversion *versus* reaction time was performed with the Au-Pd/α-MoO_3 catalyst shown in Figure 5. The conversion of cinnamyl alcohol was monitored for a period of 1 h.

When analyzing the course of the reaction between 5 and 60 min, it was found that the major product was cinnamaldehyde in the catalyst presence at all times examined. The study showed very high activity, reaching a remarkable 58% conversion in the first 10 min and exhibiting a trend after 30 min, stabilizing after this period, where a decline in benzaldehyde selectivity is observed with increasing cinnamaldehyde.

From the first 5 min of reaction, it is already possible to observe a chemoselective tendency between the two products formed. This mechanism has been previously reported by Simões *et al.*[45] In the mechanism proposed by the authors, cinnamaldehyde is formed through the

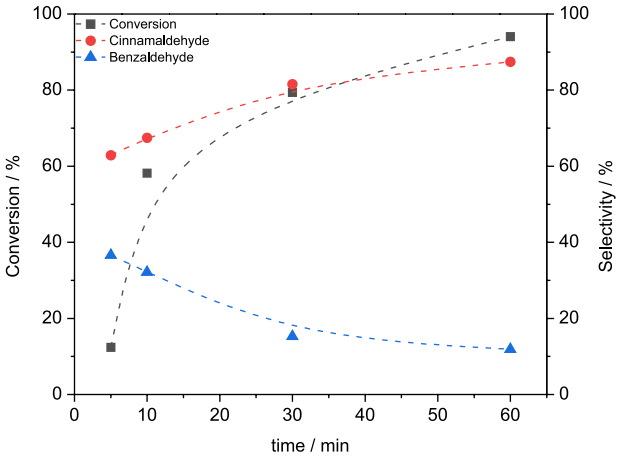

Figure 5. Influence of the reaction time on the conversion and selectivity in the oxidation of cinnamyl alcohol over Au-Pd/α-MoO_3 catalyst.

selective oxidation of the alcoholic function. At the same time, benzaldehyde is formed from side reactions via radicals. In this sense, our results suggest that the excellent performance of the catalyst in a short reaction time may be associated with the formation of higher concentrations of oxygen vacancies in the support from the electron transfers between metal-support, which may be where there is a greater influence of oxygen adsorption due to the presence of these defects that, consequently, improve the catalytic performance.[40] Thus, the efficiency of the catalyst may be associated with the oxidation state of the metals (Au^0 and Pd^0), as well as the electronic transfers between the metallic nanoparticles and Mo that activate the catalyst surface, minimizing the formation of radicals and mitigating the formation of benzaldehyde as a by-product.

In the previous work,[45] using the AgAuPd nanotube catalyst, the conversion was 77.18%, but the selectivity for cinnamaldehyde was only ca. 58.51%. The work by Rucinska *et al.*[7] showed 48% conversion and selectivity for 60% cinnamaldehyde and 28% benzaldehyde after 4 h of reaction. The results obtained here show that the presence of MoO_3 significantly increased the selectivity for cinnamaldehyde (87%). We believe that this increase in activity is related to the formation of oxygen gaps.

Recycling experiments

Recycling experiments have been proposed to evaluate the stability of the Au-Pd/α-MoO_3 catalyst. After each reaction, the catalyst was washed with CH_2Cl_2 to remove the formed organic phase and dried in an oven for 2 h. Figure 6 shows that the catalyst maintained high activity in four runs, leading to conversions of more than 80% in just 1 h, using optimized conditions for the formation of cinnamaldehyde. The catalyst did not need any addition of base or solvent to maintain its performance. The results suggest that the catalyst did not present significant deactivation processes during the studied cycles, demonstrating the possibility of being used for more cycles. To evaluate the small reduction in catalytic performance, the catalyst, after the fourth run, was analyzed by ICP-OES (Table S1, SI section). Little leaching of the active phase was verified, indicating a loss of 2% of the metallic charge concerning the fresh catalyst. The analysis also showed a greater loss of Au during the reaction cycles, which may justify the slight decrease in the conversion rate, but with a considerable control of the rates of cinnamaldehyde formed in the reaction cycles since the presence of Pd favors the selectivity of the reaction.

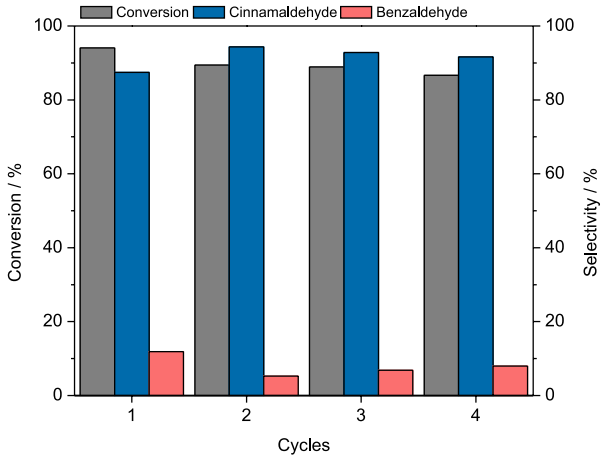

Figure 6. Recycling tests for the Au-Pd/α-MoO_3 catalyst in cinnamyl alcohol oxidation reactions under optimized conditions.

Conclusions

Au-Pd NPs were successfully deposited on the MoO_3 support using the urea precipitation deposition method, showing excellent activity for the oxidation of cinnamyl alcohol using molecular oxygen as an oxidizer under solvent or base-free conditions. The catalysts were characterized by different techniques to elucidate the characteristics of the materials and their properties. The XPS analyses indicated the presence of a redox pair Mo^{6+}/Mo^{5+} and a higher concentration of oxygen vacancies in the catalyst related to pure support. The experimental data demonstrated that the properties and characteristics of the support and the nanoparticles significantly influence the activity and selectivity in the oxidation process of cinnamyl alcohol. It was found that the presence of oxygen vacancies in the support played an important role in determining the size of the nanoparticles and in the catalytic efficiency from oxygen activation, indicating that the choice of the α-MoO_3 support was assertive due to its intrinsic properties. The Au-Pd/α-MoO_3 catalyst was stable, and it was used four times without loss of performance, maintaining selectivity for cinnamaldehyde.

Experimental

All chemicals used in the experiments were of analytical grade, bought from Sigma-Aldrich (Saint Louis, USA) and Vetec (São Paulo, Brazil), and used without further purification.

α-MoO_3 preparation

The synthesis of α-MoO_3 was followed as previously reported with some modifications.[23] In a Teflon cup, 10 g of ammonium heptamolybdate tetrahydrate $(NH_4)_6Mo_7O_{24}{\cdot}4H_2O$ (Vetec, São Paulo, Brazil) were dissolved in 60 mL of deionized water under magnetic stirring for 10 min. Then, 10 mL of an aqueous solution of hydrochloric acid (3.0 mol L^{-1}) (Sigma-Aldrich, Saint Louis, USA) was dropwise added, remaining under stirring for 10 min. At the end of the procedure, the Teflon cup was inserted into a stainless steel autoclave at 150 °C for 12 h. Subsequently, it was cooled down to room temperature, and a greenish precipitate was collected and washed three times with 40 mL of deionized water and then dried in an oven at 100 °C for 12 h. Then, the material was calcined in a muffle furnace in the air at 400 °C for 4 h, at a heating rate of 10 °C min^{-1}.

Catalyst preparation

The catalysts were synthesized using deposition-precipitation with the urea method (DPU) with some modifications as previously described.[35,46] The preparation of a catalyst with an Au:Pd molar ratio of 1:1 is described as an example: in a typical procedure, 500 mg of support (α-MoO_3) was suspended in 50 mL of deionized water and kept under magnetic stirring (800 rpm) at room temperature. Then, urea $CO(NH_2)_2$ (Sigma-Aldrich, Saint Louis, USA) was added to achieve urea to metal molar ratio of 100.[47] After 5 min, $HAuCl_4{\cdot}3H_2O$ (Sigma-Aldrich,

Saint Louis, USA) and $PdCl_2$ (Sigma-Aldrich, Saint Louis, USA) in 10 wt.% HCl were added in concentrations of 2.0 mmol L^{-1}. Next, the mixture was heated to 95 °C and kept at this temperature for 4 h under magnetic stirring, where the pH of the solution varied from 3 to 8 at the end of the process. Subsequently, the solid was collected by centrifugation, washed four times with deionized water, and dried in an oven at 70 °C. As a final step, the material was calcined at 400 °C for 6 h in a muffle furnace with a heating rate of 10 °C min^{-1}. The same procedure was used to prepare other Au:Pd molar ratios, changing the quantities of metal precursors.

Catalytic reactions

The oxidation reactions were performed in a 100 mL Fischer-Porter® glass reactor (Emper Porto Alegre, Brazil) at 4 bar of O_2 and 100 °C, except when mentioned. In a typical experiment, the reactor was loaded with the catalyst (5.3 μmol of metal) and cinnamyl alcohol (7.3 mmol) under magnetic stirring (600 rpm). The temperature and stirring were maintained by a stirring plate connected to a digital controller (Arec X, Velp Scientifica®, NY, USA). Usually, the reaction time was 1 h, although some modifications were also explored. The catalyst was separated from the products by centrifugation at the end of the reaction. For analytical analysis, 5 μL of the final solution was collected and added to 1 mL of CH_2Cl_2. The products were analyzed by gas chromatography (CG) using *p*-xylene as standard. The catalyst was washed several times with CH_2Cl_2 before each recycling for the recycling experiments.

Characterizations

Transmission electron microscopy (TEM) images were obtained using MORGAGNI 268D® (Philips, Bungkum, Bangkok) operating at 110 kV. Samples for TEM were prepared by drop-casting an isopropanol suspension of the samples over a carbon-coated copper grid, followed by drying under ambient conditions. The nanoparticles' size was determined by the ImageJ® software.[48] 130 particles were considered for that. The scanning electron microscopy (SEM) images were obtained on a Quanta 200F FEG® microscope (Fei Company, Tokyo, Japan). The X-ray diffraction (XRD) pattern was obtained on a Bruker D8 Advance® diffractometer (Bruker AXS GmbH, Karlsruhe, Germany) with Cu Kα radiation (λ = 1.5418 Å), operating at 40 kV and 40 mA, at a 2θ range from 5 to 90° with a 0.02° step size and measuring time of 5 s *per* step. The Fourier transform infrared spectroscopy (FTIR) spectra were obtained using a Spectrum 100® spectrometer (PerkinElmer, Waltham, USA), set to measure 16 cumulative scans at 4 cm^{-1} in a range between 4000 and 400 cm^{-1}. The samples were prepared as KBr pellets. Raman spectra were acquired on Bruker Senterra II® equipment coupled to an optical microscope (Bruker AXS GmbH, Karlsruhe, Germany). The samples were irradiated with the 532 nm line of a He-Ne laser. Brunauer-Emmett-Teller (BET) surface area and Barrett-Joyner-Halenda (BJH) pore size distribution on the materials were obtained on a Micromeritics ASAP 2420® equipment (Micromeritics, Florida, USA) by N_2 physisorption at 77 K. The metal content in the catalysts was determined by inductively coupled plasma optical emission spectrometer (ICP-OES) on a SPECTRO ARCOS® instrument (Spectro Arcos, trade Zone, Shanghai, China). Solid samples were first digested in a mixture of HCl and HNO_3 under heating and further diluted with deionized water. The X-ray photoemission spectra (XPS) were obtained with an ESCA+ spectrometer system (Scientia Omicron, Uppsala, Sweden) equipped with an EA 125 hemispherical analyzer and XM 1000 monochromated X-ray source in Al Kα (1486.7 eV). The X-ray source was used with a power of 280 W, as the spectrometer worked in a constant pass energy mode of 50 eV. The calibration of the XPS spectra for the charge accumulation was performed using the C 1s peak (BE = 284.8 eV). Gas chromatography analyses were performed with a Shimadzu GC-2010 gas chromatograph-flame ionization detector (FID) equipped with a capillary column Rtx-Wax 30 meters (Shimadzu Corporation, Columbia, USA). The analyses were performed under the following conditions: initial temperature 60 °C, rate 20 °C min^{-1}, final temperature 200 °C, and gas flow of 2.48 mL min^{-1}. Conversion and selectivity were calculated based on the peak areas of GC calibrated with an internal standard (*p*-xylene).

Supplementary Information

The supplementary data with N_2 adsorption/desorption isotherms, XPS standard, and ICP-OES analysis of the MoO_3 support and the Au-Pd/α-MoO_3 catalyst are available free of charge at http://jbcs.sbq.org.br as a PDF file.

Acknowledgments

The authors acknowledge financial support from CAPES. In addition, they would like to thank the Institute of Criminalistics of the State of Piauí (ICRIM-PI) for the Raman spectrophotometer and the technical support from the Center for Strategic Technology of the Northeast (CETENE-PE).

Author Contributions

Renilma C. Sousa was responsible for the investigation, data curation, writing of the original draft, and formal analysis; Jussara M. da Silva for the investigation and data curation; Jean C. S. Costa for the conceptualization and writing-review, formal analysis, funding acquisition, writing of the original draft and supervision; Carla V. R. de Moura for the conceptualization and funding acquisition. Edmilson M. de Moura for the planning, project administration, funding acquisition, writing review, and coordination.

References

1. Liu, C.-H.; Lin, C.-Y.; Chen, J.-L.; Lu, K.-T.; Lee, J.-F.; Chen, J.-M.; *J. Catal.* **2017**, *350*, 21. [Crossref]
2. Gogoi, N.; Bordoloi, P.; Borah, G.; Gogoi, P. K.; *Catal. Lett.* **2017**, *147*, 539. [Crossref]
3. Sheldon, R. A.; *Catal. Today* **2015**, *247*, 4. [Crossref]
4. Mallat, T.; Baiker, A.; *Chem. Rev.* **2004**, *104*, 3037. [Crossref]
5. Wu, P.; Cao, Y.; Zhao, L.; Wang, Y.; He, Z.; Xing, W.; Bai, P.; Mintova, S.; Yan, Z.; *J. Catal.* **2019**, *375*, 32. [Crossref]
6. Grunwaldt, J.-D.; Keresszegi, C.; Mallat, T.; Baiker, A.; *J. Catal.* **2003**, *213*, 291. [Crossref]
7. Rucinska, E.; Miedziak, P. J.; Pattisson, S.; Brett, G. L.; Iqbal, S.; Morgan, D. J.; Sankar, M.; Hutchings, G. J.; *Catal. Sci. Technol.* **2018**, *8*, 2987. [Crossref]
8. Wu, G.; Brett, G. L.; Cao, E.; Constantinou, A.; Ellis, P.; Kuhn, S.; Hutchings, G. J.; Bethell, D.; Gavriilidis, A.; *Catal. Sci. Technol.* **2016**, *6*, 4749. [Crossref]
9. Keresszegi, C.; Burgi, T.; Mallat, T.; Baiker, A.; *J. Catal.* **2002**, *211*, 244. [Crossref]
10. Haruta, M.; Kobayashi, T.; Sano, H.; Yamada, N.; *Chem. Lett.* **1987**, *16*, 405. [Crossref]
11. Hong, W.; Yan, X.; Li, R.; Fan, J.; *Chin. J. Catal.* **2017**, *38*, 545. [Crossref]
12. Lackmann, A.; Mahr, C.; Schowalter, M.; Fitzek, L.; Weissmüller, J.; Rosenauer, A.; Wittstock, A.; *J. Catal.* **2017**, *353*, 99. [Crossref]
13. Ferraz, C. P.; Garcia, M. A. S.; Teixeira-Neto, E.; Rossi, L. M.; *RSC Adv.* **2016**, *6*, 25279. [Crossref]
14. Dimitratos, N.; Porta, F.; Prati, L.; Villa, A.; *Catal. Lett.* **2005**, *99*, 181. [Crossref]
15. Gómez-Villarraga, F.; Radnik, J.; Martin, A.; Köckritz, A.; *J. Nanopart. Res.* **2016**, *18*, 141. [Crossref]
16. Wu, J.-B.; Shi, R.-P.; Qin, Z.-F.; Liu, H.; Li, Z.-K.; Zhu, H.-Q.; Zhao, Y.-X.; Wang, J.-G.; *J. Fuel Chem. Technol.* **2019**, *47*, 780. [Crossref]
17. Wu, P.; Song, L.; Wang, Y.; Liu, X.; He, Z.; Bai, P.; Yan, Z.; *Appl. Surf. Sci.* **2021**, *537*, 148059. [Crossref]
18. Greiner, M. T.; Chai, L.; Helander, M. G.; Tang, W.-M.; Lu, Z.-H.; *Adv. Funct. Mater.* **2013**, *23*, 215. [Crossref]
19. Hu, Z.; Liu, X.; Meng, D.; Guo, Y.; Guo, Y.; Lu, G.; *ACS Catal.* **2016**, *6*, 2265. [Crossref]
20. de Castro, I. A.; Datta, R. S.; Ou, J. Z.; Castellanos-Gomez, A.; Sriram, S.; Daeneke, T.; Kalantar-zadeh, K.; *Adv. Mater.* **2017**, *29*, 1701619. [Crossref]
21. Wang, L.; Wang, S.; Fu, H.; Wang, Y.; Yu, K.; *Nano* **2018**, *13*, 1850115. [Crossref]
22. Chen, D.; Liu, M.; Yin, L.; Li, T.; Yang, Z.; Li, X.; Fan, B.; Wang, H.; Zhang, R.; Li, Z.; Xu, H.; Lu, H.; Yang, D.; Sun, J.; Gao, L.; *J. Mater. Chem.* **2011**, *21*, 9332. [Crossref]
23. Pinto, B. F.; Garcia, M. A. S.; Costa, J. C. S.; de Moura, C. V. R.; de Abreu, W. C.; de Moura, E. M.; *Fuel* **2019**, *239*, 290. [Crossref]
24. Sarfraz, M.; Aboud, M. F. A.; Shakir, I.; *J. Alloys Compd.* **2015**, *650*, 123. [Crossref]
25. Parlett, C. M. A.; Durndell, L. J.; Machado, A.; Cibin, G.; Bruce, D. W.; Hondow, N. S.; Wilson, K.; Lee, A. F.; *Catal. Today* **2014**, *229*, 46. [Crossref]
26. Costa, J. C. S.; Corio, P.; Rossi, L. M.; *Nanoscale* **2015**, *7*, 8536. [Crossref]
27. Sharma, R. K.; Reddy, G. B.; *J. Appl. Phys.* **2013**, *114*, 184310. [Crossref]
28. González, J.; Wang, A. J.; Chen, L.; Manríquez, M.; Salmones, J.; Limas, R.; Arellano, U.; *J. Solid State Chem.* **2018**, *263*, 100. [Crossref]
29. Ding, Q. P.; Huang, H. B.; Duan, J. H.; Gong, J. F.; Yang, S. G.; Zhao, X. N.; Du, Y. W.; *J. Cryst. Growth* **2006**, *294*, 304. [Crossref]
30. Liu, D.; Lei, W. W.; Hao, J.; Liu, D. D.; Liu, B. B.; Wang, X.; Chen, X. H.; Cui, Q. L.; Zou, G. T.; Liu, J.; Jiang, S.; *J. Appl. Phys.* **2009**, *105*, 023513. [Crossref]
31. Mestl, G.; Ruiz, P.; Delmon, B.; Knözinger, H.; *J. Phys. Chem.* **1994**, *98*, 11269. [Crossref]
32. Dieterle, M.; Weinberg, G.; Mestl, G.; *Phys. Chem. Chem. Phys.* **2002**, *4*, 812. [Crossref]
33. Dhanasankar, M.; Purushothaman, K. K.; Muralidharan, G.; *Appl. Surf. Sci.* **2011**, *257*, 2074. [Crossref]
34. Sing, K. S. W.; Everett, D. H.; Haul, R. A. W.; Moscou, L.; Pierott, R. A.; Rouquérol, J.; Siemieniewska, T.; *Pure Appl. Chem.* **1985**, *57*, 603. [Crossref]
35. Kumar, A.; Kumar, V. P.; Srikanth, A.; Vishwanathan, V.; Chary, K. V. R.; *Catal. Letters* **2016**, *146*, 35. [Crossref]
36. Arachchige, H. M. M. M.; Zappa, D.; Poli, N.; Gunawardhana, N.; Comini, E.; *Sens. Actuators, B* **2018**, *269*, 331. [Crossref]
37. Chrouda, A.; Ahmed, S. M. A.; Elamin, M. B.; *ChemBioEng Rev.* **2022**, *9*, 248. [Crossref]
38. Méndez, F. J.; González-Millán, A.; García-Macedo, J. A.; *Mater. Chem. Phys.* **2019**, *232*, 331. [Crossref]
39. Castillo, C.; Buono-Core, G.; Manzur, C.; Yutronic, N.; Sierpe, R.; Cabello, G.; Chornik, B.; *J. Chil. Chem. Soc.* **2016**, *61*, 2816. [Crossref]

40. Khawaji, M.; Chadwick, D.; *Catal. Sci. Technol.* **2018**, *8*, 2529. [Crossref]
41. Kolodziej, M.; Lalik, E.; Colmenares, J. C.; Lisowski, P.; Gurgul, J.; Duraczyńska, D.; Drelinkiewicz, A.; *Mater. Chem. Phys.* **2018**, *204*, 361. [Crossref]
42. Cheng, H.; Qian, X.; Kuwahara, Y.; Mori, K.; Yamashita, H.; *Adv. Mater.* **2015**, *27*, 4616. [Crossref]
43. Teles, J. H.; Hermans, I.; Franz, G.; Sheldon, R. A. In *Ullmann's Encyclopedia of Industrial Chemistry*; Wiley-VCH Verlag GmbH & Co. KGaA: Weinheim, 2015, p. 1-96. [Crossref]
44. Liu, X.; Ryabenkova, Y.; Conte, M.; *Phys. Chem. Chem. Phys.* **2015**, *17*, 715. [Crossref]
45. Simões, A. M. R.; Saraiva, N. A. M.; de Moura, C. V. R.; de Moura, E. M.; Costa, J. C. S.; *Vib. Spectrosc.* **2021**, *115*, 103274. [Crossref]
46. Hermans, L. A. M.; Geus, J. W.; *Stud. Surf. Sci. Catal.* **1979**, *3*, 113. [Crossref]
47. Kolli, N. E.; Delannoy, L.; Louis, C.; *J. Catal.* **2013**, *297*, 79. [Crossref]
48. Abramoff, M. D.; Magalhaes, P. J.; Ram, S. J.; *Biophotonics Int*. **2004**, *11*, 36.

Submitted: December 14, 2021
Published online: June 30, 2022